21 May 2018

# Tutorial: Determination of Thermal Boundary Resistance by Molecular Dynamics Simulations

Zhi Liang
*Missouri University of Science and Technology*, zlch5@mst.edu

Ming Hu



## Recommended Citation

Z. Liang and M. Hu, "Tutorial: Determination of Thermal Boundary Resistance by Molecular Dynamics Simulations," *Journal of Applied Physics*, vol. 123, no. 19, article no. 191101, American Institute of Physics, May 2018.
The definitive version is available at https://doi.org/10.1063/1.5027519

Journal of Applied Physics

# Tutorial: Determination of thermal boundary resistance by molecular dynamics simulations

Cite as: J. Appl. Phys. **123**, 191101 (2018); https://doi.org/10.1063/1.5027519
Submitted: 02 March 2018 • Accepted: 19 April 2018 • Published Online: 21 May 2018

**Zhi Liang and Ming Hu**







AIP Publishing

# Tutorial: Determination of thermal boundary resistance by molecular dynamics simulations

Zhi Liang[1,a)] and Ming Hu[2,b)]
[1]*Department of Mechanical Engineering, California State University, Fresno, Fresno, California 93740, USA*
[2]*Department of Mechanical Engineering, University of South Carolina, Columbia, South Carolina 29208, USA*

(Received 2 March 2018; accepted 19 April 2018; published online 21 May 2018)

Due to the high surface-to-volume ratio of nanostructured components in microelectronics and other advanced devices, the thermal resistance at material interfaces can strongly affect the overall thermal behavior in these devices. Therefore, the thermal boundary resistance, $R$, must be taken into account in the thermal analysis of nanoscale structures and devices. This article is a tutorial on the determination of $R$ and the analysis of interfacial thermal transport via molecular dynamics (MD) simulations. In addition to reviewing the commonly used equilibrium and non-equilibrium MD models for the determination of $R$, we also discuss several MD simulation methods which can be used to understand interfacial thermal transport behavior. To illustrate how these MD models work for various interfaces, we will show several examples of MD simulation results on thermal transport across solid-solid, solid-liquid, and solid-gas interfaces. The advantages and drawbacks of a few other MD models such as approach-to-equilibrium MD and first-principles MD are also discussed. *Published by AIP Publishing*. https://doi.org/10.1063/1.5027519

## I. INTRODUCTION

When two bodies with different temperatures come into contact, heat flows from the high-temperature body to the low-temperature body. Due to the thermal resistance within the contacting materials and at the interface between two bodies, the heat flow results in temperature gradients within the two bodies, and a temperature drop, $\Delta T$, at the interface. The thermal resistance at the interface, $R$, is defined as

$$R = \Delta T/q, \tag{1}$$

where $q$ is the heat flux across the interface. If the thermal resistance at the interface is caused by imperfect contact between two surfaces, this resistance is called thermal contact resistance. Even at interfaces with perfect contact, the thermal resistance is not zero. In this case, the resistance, known as thermal boundary resistance, is due to the differences in vibrational and electronic properties between two contacting materials.

Most experimental data show that the magnitude of thermal boundary resistance typically falls between $10^{-9}$ and $10^{-7}$ m$^2$ K/W,[1] which is three to four orders of magnitude smaller than that for thermal contact resistance.[2] Although the values of typical thermal boundary resistance are very small, they are comparable to or even greater than magnitudes of thermal resistance in materials on the nanometer scale. Therefore, thermal boundary resistance cannot be neglected in the analysis of heat transfer in materials with a structure on the nanoscale, such as those in semiconductors and MEMS devices.[3–5] These nanoscale structures and devices often contain a high density of interfaces between dielectrics (e.g., silica glass, polymers, water, air, etc.) or semiconductors. The main thermal energy carriers across such interfaces are phonons. In this case, the thermal boundary conductance, $G$ (the inverse of thermal boundary resistance), can be estimated by the summation of all phonon contributions using[6]

$$G = \frac{1}{2}\sum_j \int_0^{\pi/2}\int_0^{\omega_1^{\max}} d\omega \frac{\omega^2}{2\pi^2 c_j^3}\frac{df_j(\omega,T)}{dT} \times \hbar\omega c_{1,j}\cos\theta_1 \alpha_{1\to2}(\theta_1, j, \omega)\sin\theta_1 d\theta_1, \tag{2}$$

where $\omega$ is the phonon frequency, $\theta$ is the angle between the normal to the interface and the phonon propagation direction, $\omega^{\max}$ is the maximum phonon frequency, $T$ is the temperature, $\hbar$ is the Planck constant divided by $2\pi$, $c$ is the phonon group velocity, $\alpha$ is the phonon transmission coefficient, and $f$ is the phonon occupation number. In Eq. (2), subscripts 1 and 2 denote material 1 and material 2, respectively, that comes into contact and forms an interface. Subscript $j$ is the phonon branch.

A key parameter in Eq. (2) to evaluate the thermal boundary conductance, $G$, is the phonon transmission coefficient, $\alpha$, which is defined as the ratio of the transmitted phonon energy to the incident phonon energy. There are two theoretical models that are commonly used to predict $\alpha$ and understand interfacial phonon transport physics. One is the acoustic mismatch model (AMM), which assumes specular reflection and refraction of phonons at the interface (see Fig. 1). In the AMM, $\alpha$ is determined by[6]

$$\alpha_{1\to2} = \frac{4z_1 z_2\cos\theta_1\cos\theta_2}{(z_1\cos\theta_1 + z_2\cos\theta_2)^2}, \tag{3}$$

where $z_1 = \rho_1 c_1$ and $z_2 = \rho_2 c_2$ are the acoustic impedances, $\rho_1$ and $\rho_2$ are the densities, and $\theta_1$ and $\theta_2$ are related by Snell's law as $\sin\theta_1/c_1 = \sin\theta_2/c_2$. The AMM is valid for

a)Electronic mail: zliang@csufresno.edu
b)Electronic mail: minghu@cec.sc.edu

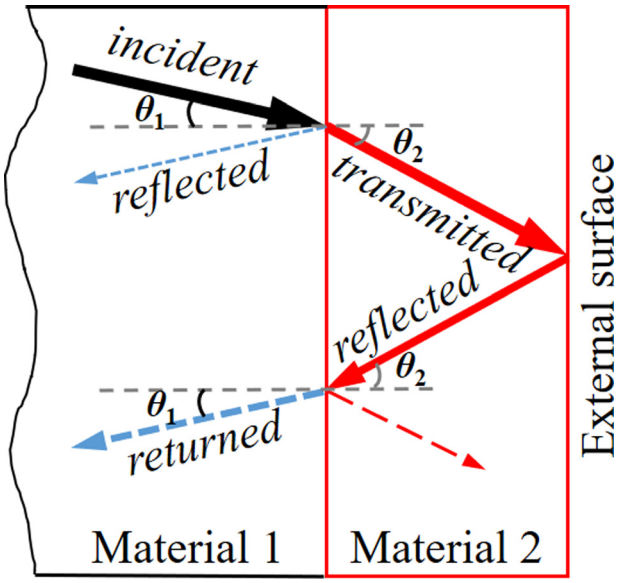


FIG. 1. Schematic diagram of specular phonon refraction and reflection at the material interface and external surface.

high-quality interfaces and for phonon wavelength much greater than typical interatomic spacing. For the interaction between phonons and real interfaces, however, diffuse scattering of phonons [i.e., acoustic correlations given by Eq. (3) are destroyed] was detected by experiment.[7] To account for the effect of diffuse phonon scattering, Swartz[8] proposed the diffuse mismatch model (DMM) which assumes that all the phonons are diffusely scattered at the interface. The only difference between the DMM and the AMM is the phonon transmission coefficient.[6] In the DMM, $\alpha$ is determined by mismatch between phonon density of states (DOS)[8]

$$\alpha_{1\to 2}(\omega) = \frac{\sum_j c_{2,j} D_{2,j}(\omega, T)}{\sum_j \left[c_{1,j} D_{1,j}(\omega, T) + c_{2,j} D_{2,j}(\omega, T)\right]}, \quad (4)$$

where $D$ is the phonon DOS per unit volume. Under the Debye approximation for phonon velocities and phonon DOS, $\alpha$ is independent of temperature and strength of interfacial bonding.

The assumption of complete diffuse scattering (i.e., all incident phonons lose memory of where they came from) at the interface in the DMM is the opposite extreme of the complete specularity assumption in the AMM. The actual degree of diffuse phonon scattering at interfaces depends on many interface parameters such as interfacial structure,[9–12] strength of interfacial bonding,[12–15] temperature,[16–18] pressure,[19–21] etc. Hence, the phonon interaction with real interfaces is much more complex than the simple pictures described by the two models. In addition, both the AMM and the DMM assume elastic scattering (i.e., the transmitted and reflected phonons have the same frequency as the incident phonon) at the interface, which leads to a prediction of temperature-independent thermal boundary resistance in the classical limit. This prediction contradicts numerous experimental findings showing that thermal boundary resistance decreases with increasing temperature in the classical limit.[16–18] The temperature-dependent experimental results are attributed to the increase in inelastic phonon scattering at the interface, which are not accounted for in the AMM and the DMM.

A more realistic method to investigate the thermal transport across interfaces is the molecular dynamics (MD) simulation. In an MD simulation, one can follow trajectories, velocities, and forces of all atoms and molecules in the system by numerical integration of Newton's equation of motion. Via statistical mechanics based molecular-level formulas and time averaging, one can determine macroscopic equilibrium and transport properties. The forces between atoms are normally derived from empirical interatomic potentials. MD simulations require no assumption about the nature of the phonon scattering and hence account for both the elastic and inelastic scattering of phonons at the material interface. Due to this advantage, MD simulations are capable of predicting a temperature-dependent thermal boundary resistance,[18,22] which is consistent with experimental data. Furthermore, MD simulations are able to build well-controlled interfaces at the atomic level.[22–28] With this advantage, MD simulations are able to study the effects of the interfacial structure, bonding strength, pressure, etc., on thermal boundary resistance. All these effects are not accounted for by the original AMM and DMM.

Due to the aforementioned merits, MD simulations are widely used in the investigation of thermal boundary resistance. Since MD simulations use Newton's equation of motion that does not take into account the quantum effects of phonon properties, they are only valid within the classical limit. This imposes a restriction on the application of MD simulations. Below the Debye temperature, the quantum effects of phonons become important. MD predictions of thermal boundary resistance can be inaccurate at these low temperatures.

In this tutorial, we focus on the determination of thermal boundary resistance and analysis of interfacial phonon transport physics via MD simulations. The rest of the tutorial is arranged as follows: In Sec. II, we describe the commonly used MD methods for the determination of thermal boundary resistance and methodology for the analysis of interfacial phonon scattering. In Sec. III, we present typical MD simulation results on thermal boundary resistance at various interfaces. In Sec. IV, we discuss several other MD simulation methods and their advantages and drawbacks. Finally, we close with a summary.

## II. MD SIMULATIONS

### A. Non-equilibrium MD (NEMD) determination of *R*

The most popular method in MD determination of thermal boundary resistance, $R$, is non-equilibrium MD (NEMD) simulations. In NEMD simulations, the model structure is first equilibrated to a desired temperature and pressure, and then a heat source and a heat sink are introduced on, respectively, one side and the other side of the interface to generate a heat flux across the interface (e.g., Fig. 2). After the system reaches a steady state, the thermal boundary resistance is directly determined by Eq. (1).

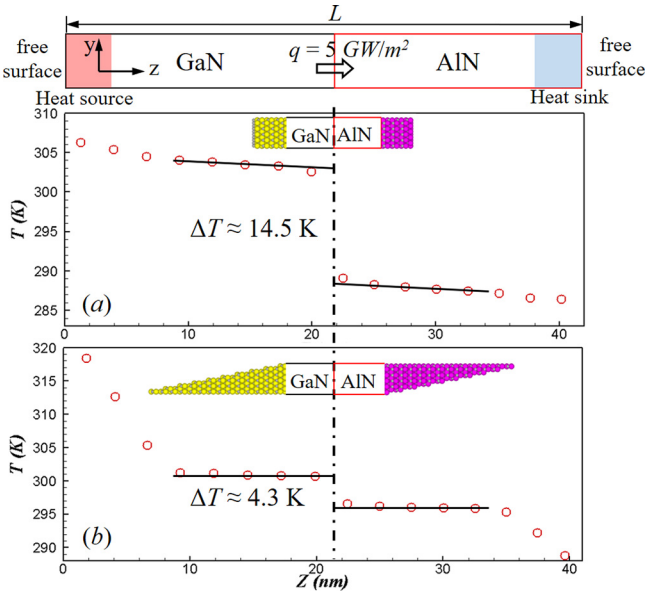


FIG. 2. NEMD simulation cell containing an epitaxial interface formed by a GaN lead and an AlN lead and temperature profiles obtained from the NEMD simulation for a structure with (a) smooth and (b) very rough external surfaces (Ref. 10). Reproduced with permission from Z. Liang and P. Keblinski, Phys. Rev. B **90**, 075411 (2014). Copyright 2014 American Physics Society.

If a heat flux is applied in the NEMD simulation by adding a constant amount of energy, $\Delta E$, to the heat source and removing the same amount of energy from the heat sink at each time step, $\Delta t$, the heat flux can be directly determined by $q = \Delta E/(A\Delta t)$, where $A$ is the cross section area. Alternatively, one can generate a heat flux by maintaining a higher temperature in the heat source and a lower temperature in the heat sink using the velocity rescaling method[29] or a thermostat.[30–32] In this case, one should monitor the energy input to the heat source and heat sink and calculate the time-averaged heat flux, $q$, for determining the thermal boundary resistance. To find the temperature drop, $\Delta T$, at the interface, the temperature profile in the heat flow direction is calculated after the system reaches steady state. By extrapolating the temperature profiles in the two materials to the interface, $\Delta T$ at the interface can be evaluated [e.g., Fig. 2(a)]. Usually, the temperature points near the heat source and heat sink regions and those adjacent to the interface are ignored in a linear fit to the temperature profile as they are generally nonlinear. Since too low a $q$ can be insufficient to establish a visible temperature drop at the interface, and too high a $q$ can cause nonlinear response of $\Delta T$ to $q$ and even sublimation of the system, the effects of the value of $q$ on thermal boundary resistance, $R$, should be studied for the selection of an appropriate value of $q$ for the prediction of $R$.

### B. Finite size effects on NEMD prediction of *R*

Due to the restriction of computational power, most of the model structures in NEMD prediction of $R$ contain less than $10^6$ atoms. This limits the dimension of the simulation cell to be less than ~100 nm in each direction. The nanoscale confinement in the model structure could induce finite size effects on NEMD determination of $R$, especially for a structure containing crystals with a long phonon mean free path (MFP). To determine the $R$ of an isolated interface using NEMD simulations, therefore, the finite size effect must be removed.

If the size of the simulation cell is very small, the artificial confinement in the model structure results in a very coarse Brillouin-zone (BZ) resolution. Accordingly, very few phonon modes are available to reproduce actual phonon scattering present at the interface, and MD predictions of $R$ becomes inaccurate.[18,22] To remove this effect, one can gradually increase the simulation system size until there is no significant size effect on $R$. Perpendicular to the heat flow direction, four to six unit cells, along with the periodic boundary conditions (PBCs), are usually enough to remove artifact associated with the coarse BZ resolution. Along the heat flow direction, there is another finite size effect which is in fact a combined effect of internal and boundary scattering.[10,33] As shown in Fig. 1, when the length of materials forming the interface is less than the bulk phonon MFP, the phonons transmitted from material 1 to material 2 have a high probability to travel ballistically in material 2. If the external surface of material 2 is atomistically smooth, which is the case in most NEMD simulations of interfacial thermal transport, the phonons can be specularly reflected by the smooth external surface and returned to material 1 without energy transfer. This in turn effectively reduces the phonon transmission coefficient and increases $R$.

Based on this mechanistic understanding, there are two approaches to remove the size effect on NEMD prediction of $R$. One approach that is widely used in the literature is to gradually increase the length, $L$, of the model structure until there is no significant size effect on $R$. As $L$ increases, the transmitted phonons have a higher probability to be diffusely scattered in the material, and thus, less phonons can travel ballistically to the external surface and be transmitted back without energy transfer. Accordingly, the effective phonon transmission coefficient increases and $R$ decreases with increasing $L$. An example of size-dependent $R$ obtained from NEMD simulations is shown in Fig. 3. A similar size dependence of $R$ can be also found in the literature for systems with fixed boundaries[18,34] and with PBCs[35] in the heat flow direction. To predict the value of $R$ in the limit of $L \rightarrow \infty$, i.e., $R$ of the isolated interface, one can fit the $R$ vs. $1/L$ data points with a linear function and extrapolate it to an infinite system size.[10,33,34] Alternatively, one can increase $L$ to a value much greater than the bulk phonon MFP such that the size effect on $R$ becomes negligible.[11,18,22] For interfaces formed by materials with short bulk phonon MFPs, therefore, one can obtain an asymptotic $R$ corresponding to the characteristics of an isolated interface with a relatively small system size and a low computational cost. If the interface is formed by highly conductive materials, such as Si, GaN, and AlN whose bulk phonon MFP could reach hundreds of nanometers[26,33] near room temperature, however, the computational cost could be very high to obtain a size-converged $R$ using the aforementioned approach.

The second approach to eliminate the size effect is to introduce a very rough external surface which scatters most phonons diffusely. In this case, even if the simulation cell size is small and the transmitted phonons travel ballistically

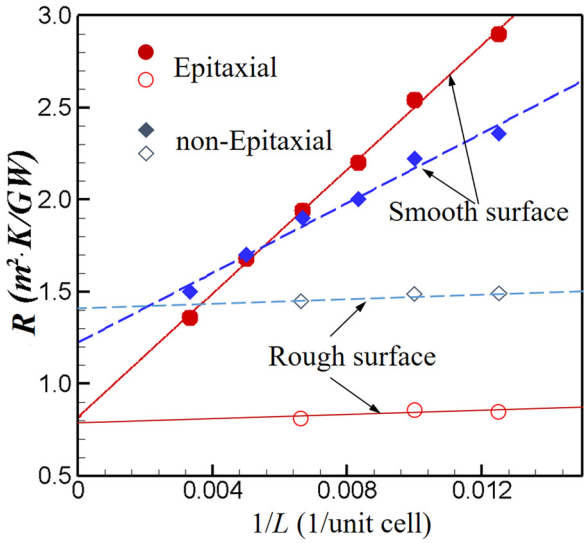


FIG. 3. $R$ as a function of $1/L$ for an epitaxial GaN|AlN interface involving smooth external surfaces (filled circles), an epitaxial interface involving very rough external surfaces (open circles), a nonepitaxial interface involving smooth external surfaces (filled diamonds), and a nonepitaxial interface involving very rough external surfaces (open diamonds). The lines show fitting of the data by linear functions (Ref. 10). Reproduced with permission from Z. Liang and P. Keblinski, Phys. Rev. B **90**, 075411 (2014). Copyright 2014 American Physics Society.

to the external surface, phonons will be thermalized at the external surface instead of being reflected and transmitted back without energy transfer. With a very rough external surface, therefore, essentially no transmitted phonons can be transmitted back, and thus one can obtain a size-converged $R$ with a system size several times smaller than MFP. For instance, it is clearly shown in Fig. 2 that $R$ at a GaN|AlN epitaxial interface is strongly affected by the external surface roughness when the system size is small. Furthermore, it is shown in Fig. 3 that if a very rough external surface is used, $R$ is essentially size independent and its value is close to the extrapolated value of $R$ with smooth external surfaces in the limit of $L \to \infty$. These results indicate that introduction of the rough surfaces is a much more robust and efficient method to suppress the size effects.

The size effect on MD prediction of $R$ is also affected by the degree of diffuse phonon scattering at the interface. For example, due to atomic restructuring and dislocations at the non-epitaxial GaN|AlN interface, the phonon scattering at the non-epitaxial interface is more diffuse (i.e., more incident phonons lose memory of where they came from) than that at an epitaxial interface.[10] Figure 3 shows that the size effect on $R_{\text{non-epitaxial}}$ ($R$ at the non-epitaxial GaN|AlN interface) is smaller than that on $R_{\text{epitaxial}}$ ($R$ at the epitaxial GaN|AlN interface). The size effect on $R_{\text{non-epitaxial}}$ can also be eliminated by introducing very rough external surfaces. In the limit of infinite system size, it is seen from Fig. 3 that $R_{\text{non-epitaxial}}$ is higher than $R_{\text{epitaxial}}$. Due to the smaller size effect on $R_{\text{non-epitaxial}}$, however, it is shown in Fig. 3 that $R_{\text{non-epitaxial}}$ could be lower than $R_{\text{epitaxial}}$ if the system size is small. Due to the size effect, therefore, opposite conclusions could be drawn at different system lengths. This result suggests caution in interpreting MD simulation results of $R$ where the system size is not long enough to eliminate the size effect.

### C. Equilibrium MD (EMD) determination of *R*

While the NEMD method allows determination of the value of $R$, detailed understanding of the thermal coupling across the interface can be obtained from the equilibrium MD (EMD) simulations.[36] After the simulation system reaches thermal equilibrium at a given temperature $T$, the EMD method uses the fluctuations of heat power across the interface to compute $G$ (inverse of $R$) via the fluctuation-dissipation theorem and the Green-Kubo formula[37]

$$G = \frac{1}{Ak_BT^2}\int_0^\infty \langle P(t)P(0)\rangle dt, \tag{5}$$

where $\langle\cdots\rangle$ means ensemble average, $A$ is the cross section area of interface, $k_B$ is the Boltzmann constant, and $P$ is the fluctuating heat power across the interface which can be computed by

$$P(t) = dE_i(t)/dt, \tag{6}$$

where $E_i(t)$ is the internal energy of the material on one side of the interface at time $t$. In the calculation of heat power across the interface, one can decompose the interatomic interaction into two-body and three-body interactions (if any).[38] This can help understand the major contribution to the interfacial heat flux.

It was pointed out by Barrat and Chiaruttini[39] that the Green-Kubo relation shown in Eq. (5) is only valid for an infinite system where the heat capacity of the two materials forming the interface, $C_V \to \infty$. However, the model system in MD simulations is always finite. For a finite system, the $G$ relates to the long-time integral of $\langle P(t)P(0)\rangle$ by[39]

$$Ge^{-at_s} = \frac{1}{Ak_BT^2}\int_0^{t_s} \langle P(t)P(0)\rangle dt, \tag{7}$$

where $a = AG/C_V$, $t_s$ is the integration time. Therefore, due to the finite size of the simulation system, the running integral $\int\langle P(t)P(0)\rangle dt$ will exhibit an exponential decay at long times which contains the information on $G$. Only in special cases where $G$ is very small or $C_V$ is very large, which makes $e^{-at} \approx 1$, the running integral $\int\langle P(t)P(0)\rangle dt$ may contain an initial plateau part which can be used to evaluate $G$.[39,40] The Green-Kubo relation based EMD method has been successfully used to determine thermal boundary resistance at various solid-solid, solid-liquid, and solid-gas interfaces.[10,14,38–41]

For example, Fig. 4(a) shows the running integral of the autocorrelation function of heat power across an epitaxial GaN|AlN interface at a temperature of 300 K. After the initial 2 ps of very large oscillations, the running integral exhibits a monotonic decay until ~15 ps. After 15 ps, the running integral exhibits a slower decay mixed with oscillations. The MD simulation results showed that the period of these oscillations increases with increasing the system length, and that it is consistent with the average time for acoustic phonons to travel back and forth in the structure for one period.[10] Therefore, these oscillations are thought to be caused by echoes of phonon reflection from the external surfaces. Similar oscillations in the tail of the running integral were also

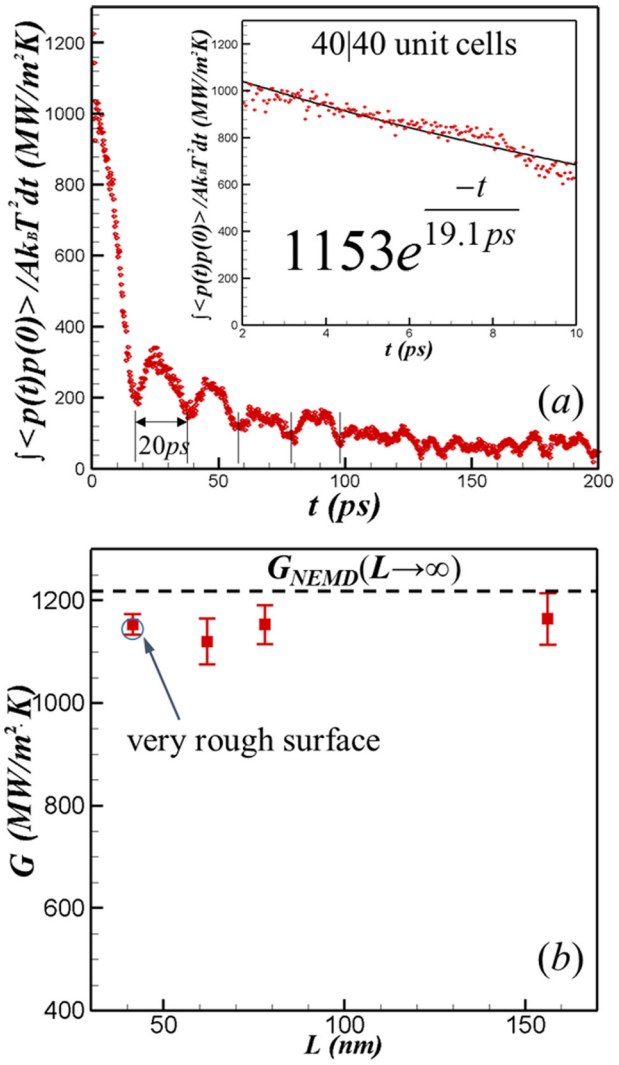


FIG. 4. (a) The running integral of time correlation function in a 40|40-unit-cell GaN|AlN structure involving smooth external surface. The inset shows an exponential fit to the initial part of the running integral. (b) EMD prediction of $G$ as a function of system length. The horizontal dashed line indicates the value of $G$ from NEMD simulation in the limit of infinite system size (Ref. 10). Reproduced with permission from Z. Liang and P. Keblinski, Phys. Rev. B **90**, 075411 (2014). Copyright 2014 American Physics Society.

observed in EMD prediction of $G$ at an interface between two Lennard-Jones (LJ) crystals.[41] Since these oscillations are associated with the artificial size effect of the model system, only part of the running integral, in which the echoes are not observed yet, should be used to determine $G$ from the EMD simulation. It is shown in the inset of Fig. 4(a) that the running integral of initial 2 to 10 ps can be well fitted by an exponential function. Using the relation in Eq. (7), the exponential fit gives $G \approx 1.15\,\mathrm{GW/m^2\,K}$, which is close to $G \approx 1.22\,\mathrm{GW/m^2\,K}$ in the limit of the infinite system size from the NEMD method. As shown in Fig. 4(b), when the finite size effects are treated properly, the $G$ predicted by the EMD method is essentially size independent and is close to size-converged $G$ obtained from the NEMD method.

After the value of $G$ or $R$ is determined from MD simulations, it is important to access the validity and accuracy of predictions from MD simulations by comparing the MD results with experimental values and theoretical predictions. The experimental value of $G$ at the GaN|AlN interface, which was derived from thermal conductivity measurement of $(AlN)_{4.1\,nm}$–$(GaN)_{55\,nm}$ superlattices, was found to be $\sim 0.62\,\mathrm{GW/m^2\,K}$.[42] It was pointed out by Koh *et al.* that the GaN|AlN interface in the experiment might not be perfectly smooth, and $G$ could be larger for smoother interfaces. Using the AMM, Koh *et al.* estimated that $G$ at a smooth GaN|AlN interface is $1.4\,\mathrm{GW/m^2{\cdot}K}$.[42] Since the interface in our model structure is perfectly smooth, the value of $G$ predicted by MD simulations is in reasonable agreement with the experimental values and the theoretical prediction.

Although numerous studies show that reliable and consistent predictions of $G$ can be obtained by both EMD and NEMD methods,[10,14,38–40] the determination of $G$ by the EMD method is not so straightforward as that by the NEMD method in many applications. To properly extract $G$ from the time integral of the correlation function, careful consideration must be given to effects associated with finite heat capacity of the simulation domain[10,14,39] and phonon scattering from the external surfaces.[10] Moreover, the appropriate definition of the position of the interface is also important for the correct determination of $G$ from EMD simulations when the interface is rough or there is an adsorbed layer at the solid-fluid interface. For example, recent studies[14] show that if adsorbed layers are formed at solid-gas interfaces, the interface must be defined at a plane out of the outmost adsorbed layer to obtain the correct result from the EMD simulation. By contrast, the precise definition of the location of the interface is not that consequential for the correct evaluation of $G$ from the NEMD method as long as it is near the location where the two materials are in contact.

### D. Analysis of interfacial phonon scattering via MD simulations

Despite tremendous efforts that have been dedicated to predict thermal transport (mainly to determine the value of $R$ or $G$) across various interfaces in the past few decades by classical MD simulations, limited progress has been made in analyzing the detailed mechanism of interfacial phonon transport, in particular at the phonon frequency or mode level. The scientific challenge resides in the precise description of behavior of phonon modes near the interface region. The traditional physical concept of phonons can be only well defined in the perfect periodic lattice. Obviously, the interface, which consists of two or more different materials in contact, lacks of such periodicity in this sense. Therefore, the recently well-developed phonon transport theory and/or methods, for instance the Boltzmann transport equation (BTE) approach, cannot be simply transferred to interface problems. This in turn requires the researchers to develop more sophisticated approaches that do not strictly rely on the traditional definition of phonons (i.e., lattice vibration). Below we introduce a few methods that have been developed to analyze the interfacial thermal transport phenomena.

#### 1. Wave packet dynamics (WPD) simulation

The first effective approach to study the interfacial phonon transport is the phonon wave packet dynamics (WPD)

simulation, which was originally proposed by Schelling *et al.*[43,44] In the WPD simulation, one should first relax the entire structure including interfaces at 0 K by minimizing the potential energy of the system with respect to atomic coordinates. Then, a phonon wave packet (WP) with a pre-defined wavevector and polarization is launched in the crystalline material (material 1) that is on the one side of the interface to be studied. To generate a phonon WP centered at a wavevector $k_0$ in the $\lambda$ branch, and localized in space around $z_0$ with a spatial extent of $\sim 1/\eta$, one can displace the atoms in materials 1 according to[10,43]

$$u_l^{\alpha}(s) = \frac{1}{\sqrt{M_s}} A_{\lambda \vec{k}_0} \varepsilon^{\alpha}_{\lambda \vec{k}_0}(s) e^{ik_0(z_l - z_0)} e^{-\eta^2 (z_l - z_0)^2}, \tag{8}$$

where $u_l^{\alpha}(s)$ represents the $\alpha$ component of displacement of atom $s$ in primitive cell $l$ of material 1, $M_s$ is the mass of atom $s$, $A_{\lambda k0}$ is the amplitude of the wave, $\varepsilon_{\lambda k0}{}^{\alpha}(s)$ is the $\alpha$ component of the eigenvector of atom $s$ for $\lambda$ branch at $k_0$, and $z_l$ is the z coordinate of the primitive cell $l$. The eigenvector $\varepsilon_{\lambda k0}{}^{\alpha}(s)$ in Eq. (8) and the corresponding eigenvalue $\omega_{\lambda k0}$ are obtained by diagonalizing the dynamical matrix of material 1. The force constants in the dynamical matrix are determined from the second order derivatives of potential energy.

To form a WP that is localized in both real space and wavevector space as described in Eq. (8), the initial atomic displacements are expressed in terms of linear combination of vibrational eigenstates[10,44]

$$u_l^{\alpha}(s) = \frac{1}{\sqrt{NM_s}} \sum_{\lambda \vec{k}} A_{\lambda \vec{k}} \varepsilon^{\alpha}_{\lambda \vec{k}}(s) e^{ik(z_l - z_0)}, \tag{9}$$

where $N$ is the number of primitive cells in material 1. In Eq. (9), the amplitude of each vibrational normal mode, $A_{\lambda k}$, is determined by the inverse Fourier transform of the function in Eq. (8). To determine initial atomic velocities, one should add time dependence, $e^{-i\omega t}$, to the displacements in Eq. (9) and differentiate it with respect to time. Accordingly, the initial velocities are given by[10]

$$\dot{u}_l^{\alpha}(s) = \frac{1}{\sqrt{NM_s}} \sum_{\lambda \vec{k}} -i\omega_{\lambda \vec{k}} A_{\lambda \vec{k}} \varepsilon^{\alpha}_{\lambda \vec{k}}(s) e^{ik(z_l - z_0)}, \tag{10}$$

where $\omega_{\lambda k}$ is the eigenvalue for the $\lambda$ branch at wavevector $k$.

With the initial atomic displacements and velocities given by Eqs. (9) and (10), one can run an MD simulation and monitor how the launched WP propagates in the model structure and interacts with the interface. After arriving at the interface, a part of the energy of the incident WP is transmitted and the rest is reflected. The analysis of these energies allows calculation of the transmission coefficient for the given phonon WP. Care must be taken when choosing the length of the crystalline material where the WP is launched. The length should be sufficiently long to study the transmission of the WP across the interface without interference from boundary scattering. One should also verify that the final result of the transmission coefficient should not depend on the spatial width and the amplitude of the initial WP.

For example, the WPD simulation was used to study phonon transport across the crystalline-Si|amorphous-$SiO_2$ ($c$-Si|$a$-$SiO_2$) interface.[45] In the WPD simulation, a WP is launched in the center of the Si crystal with a spatial extent, $1/\eta \approx 22$ nm. Figure 5 shows snapshots of spatial distribution of $v_x$ (atomic velocity in the x-direction) in the Si|$a$-$SiO_2$ structure for a transverse acoustic (TA) WP centered at 1.00 THz. It is seen that the WP travels in the z-direction and the phonon transmission and reflection at the interface completed within 20 ps. The phonon transmission coefficient, $\alpha$, can be determined by computing the internal energy in the Si crystal before the WP arrives at the interface (incident energy) and after the WP is reflected (reflected energy). Using the similar WPD simulation, one can launch phonon WPs with different frequencies and modes and determine $\alpha$ of each WP. Figure 6 shows the frequency-dependent $\alpha$ at the Si|$a$-$SiO_2$ interface for both TA and longitudinal acoustic (LA) phonons. At the lowest simulated frequency, the WPD simulation predicts $\alpha_{LA} = 0.98$ and $\alpha_{TA} = 0.95$. These values agree very well with $\alpha_{LA} = 0.98$ and $\alpha_{TA} = 0.94$ predicted by the AMM [Eq. (3)] for phonons arriving normal to the Si|$a$-$SiO_2$ interface. The simulation results indicate that the scattering of low-frequency phonons at the Si|$a$-$SiO_2$ structure is essentially specular. As the phonon frequency increases, Fig. 6 shows that the transmission coefficient decreases rapidly

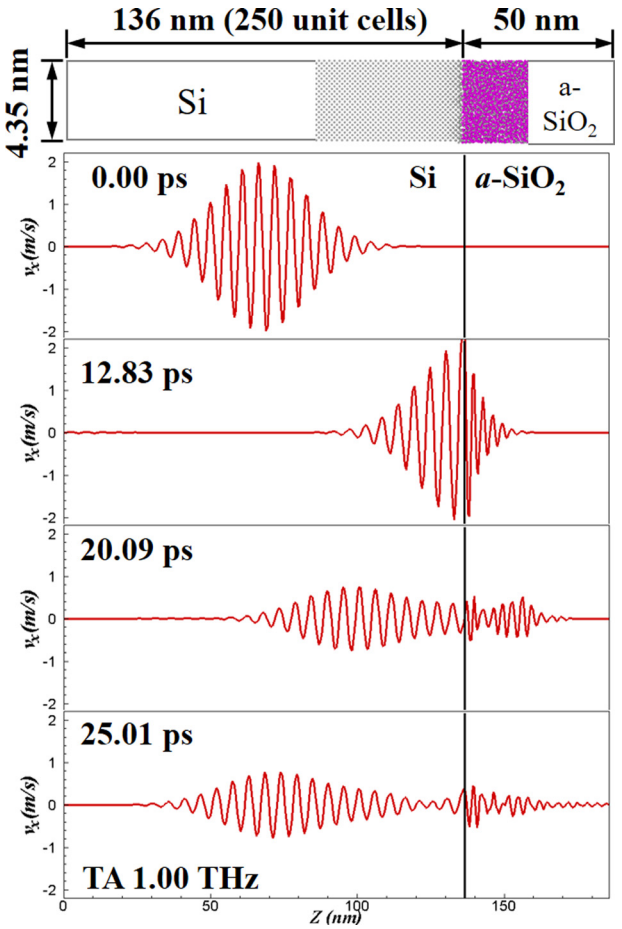


FIG. 5. Snapshots of spatial distribution of $v_x$ in the Si|$a$-$SiO_2$ structure for a TA mode phonon WP with $\nu = 1.00$ THz obtained from the WPD simulation (Ref. 45). Reproduced with permission from Z. Liang and P. Keblinski, Phys. Rev. B **93**, 054205 (2016). Copyright 2016 American Physics Society.

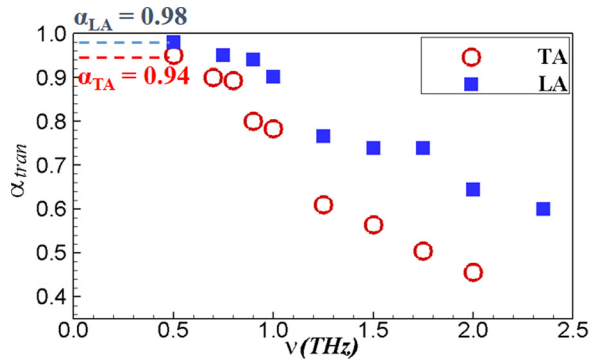


FIG. 6. WPD simulation results of the transmission coefficient at the Si|$a$-$SiO_2$ interface for TA and LA phonons as a function of phonon frequency. The dashed lines indicate the transmission coefficients predicted by the AMM (Ref. 45). Reproduced with permission from Z. Liang and P. Keblinski, Phys. Rev. B **93**, 054205 (2016). Copyright 2016 American Physics Society.

to a value much lower than predictions from the AMM. This indicates that the interfacial scattering becomes more diffuse for high-frequency phonons.

With the frequency-dependent transmission coefficient obtained from WPD simulations, an estimate of the magnitude of thermal boundary resistance, $G$, can be made using Eq. (2). The estimated $G$ can be then compared to the results directly from the EMD or NEMD simulations described in Secs. II A and II C. It was shown by Deng *et al.*[46] that WPD and NEMD approaches predict similar values for $G$ at the Si|$a$-$SiO_2$ interface and the predicted value is also consistent with the experimental results.

It should be noted that, so far WPD simulations were all carried out at a temperature of 0 K, and consideration of intrinsic anharmonic effect in phonon-phonon scattering (such as phonon scattering at finite temperatures) and phonon-structure interaction in WPD simulation is still missing. Nevertheless, one can still gain much knowledge of the dominant phonon-interface interaction process for most of the cases by analyzing the transmitted/reflected energy distribution, mode conversion, etc. Diverse interface conditions such as non-bonding vs. bonded interface,[47,48] smooth vs. rough surfaces,[49] and interface between crystalline and amorphous structures[49,50] can be fully considered and studied at the atomistic level. In addition to the transmission coefficient, one can also visualize the detailed phonon-interface or phonon-boundary scattering process from the WPD simulation.

### 2. Approaches based on EMD simulations

So far, the application of WPD simulation is mainly limited to systems or interfaces where the anharmonic effect is not strong. However, there are lots of materials or interfaces having strong intrinsic anharmonicity. To this end, an intuitive idea is to extract phonon information from direct EMD simulations at finite temperatures. Rigorous calculation of individual phonon mode contribution to the overall thermal transport based on EMD simulations has become available, namely, the spectral energy density (SED)[51] or equivalently the time domain normal mode analysis (TDNMA)[52] methods. They have successfully predicted the phonon behavior in perfect bulk systems, e.g., mode specific phonon lifetime. By making some assumptions, they can also be used to deal with complicated systems, such as superlattices[53] and alloys,[54] where the entire period or simulation cell is treated as a "super" unit cell. Despite its success, the SED method is not efficient to process large inhomogeneous systems, including interfaces.

In an attempt to study complicated systems without involving a "super" unit cell, Chalopin *et al.*[38] formulated thermal boundary conductance within the framework of the linear response theory and presented an approach to retrieve thermal boundary conductance from EMD simulations with the model system of the Si/Ge superlattice. The results of this method also demonstrate that coherency effects are less important compared with anharmonicity of interfaces. Later, Chalopin and Volz[55] presented a microscopic approach to predict the frequency vs. wave-vector dependent phonon transmission across a solid-solid interface. The spectral heat flux is deduced from the equilibrium displacement fluctuations of the atoms near the interface. They ran a model system of Si/Ge slabs in contact within EMD and compared the thermal boundary conductance with that directly from the NEMD method. They demonstrate the existence of a localized, non-dispersive, and directional interface mode which contributes largely to the heat transfer between Si and Ge.

Another way of understanding the interfacial thermal transport is by analyzing vibrational density of states (VDOS), i.e., number of vibrational modes per unit volume and frequency, in the two materials forming the interfaces. The phonon transport across an interface is strongly influenced by the mismatch in the vibrational properties of the materials in contact.[6] In the DMM, the phonon transmission coefficient is given by the differences in VDOS [i.e., Eq. (4)]. To numerically analyze the vibrational properties, the VDOS in materials on each side of the interface is usually quantified via a Fourier transform of the atomic velocity autocorrelation function (VAF)[56]

$$D(\omega) = \int_0^\infty \langle \vec{v}(t)\vec{v}(0)\rangle e^{i\omega t} dt, \tag{11}$$

where $D(\omega)$ is the VDOS at frequency $\omega$ and $v$ is the atomic velocity. The VAF is normally obtained from EMD simulation of the model system.

A large overlap between the VDOSs in materials on two sides of the interface implies strong vibrational coupling and, consequently, a low thermal boundary resistance. Hence, comparing the overlap between the VDOSs in some specific frequency regions can help understand the variation in thermal boundary resistance under different interface conditions. For example, Hu *et al.*[57] have successfully used the VDOS mismatch to explain the enhanced overall thermal boundary conductance across the confined AlN layer between GaN and SiC in terms of the phonon bridging effect. Figure 7 shows that there is a large VDOS mismatch between the Si atoms in SiC and the Ga atoms in GaN. The confined nanoscopic AlN layer serves as a phonon bridge to connect GaN and SiC surfaces. The VDOS of Al and N atoms in the low frequency region falls between that for Ga and Si. Such VDOS match facilitates interfacial thermal

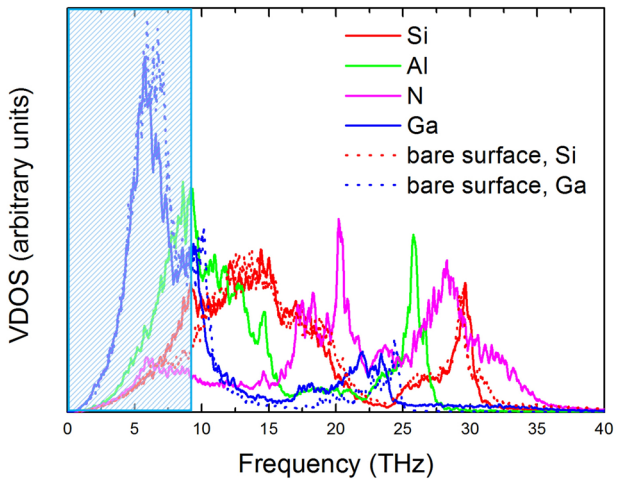


FIG. 7. Comparison of vibrational density of states between GaN|SiC interface with a 1 unit cell non-epitaxial AlN layer (solid lines) and bare GaN|SiC surface (dotted lines). The shaded area shows better VDOS match between confined AlN and neighboring GaN and SiC (Ref. 57). Reproduced with permission from M. Hu, X. Zhang, D. Poulikakos, and C. P. Grigoropoulos, Int. J. Heat Mass Transfer **54**, 5183 (2011). Copyright 2011 Elsevier Publishing.

transport, since low frequency phonons conduct heat more efficiently. The MD simulation demonstrated that the overall thermal boundary conductance is significantly enhanced by adding a very thin AlN layer between GaN and SiC. This demonstrates that adding a third material of thickness on the order of nanometer scale could enhance the thermal transport across the interface, as opposite to the traditional thermal interface materials (TIMs) which always bring additional thermal boundary resistance.

### 3. Approaches based on NEMD simulations

In the framework of NEMD, recently Zhou *et al.*[58] reformulated the MD expression of heat current that was originally derived by Irving and Kirkwood[59] and later extended by Torii and Ohara *et al.*,[60,61] by expressing the atomic velocity and displacement using the theory of lattice dynamics. This method is called the time domain direct decomposition method (TDDDM), which can be used to predict the phonon mode specific thermal conductivity.[58] Later, Zhou and Hu[62] proposed a new computational scheme, called the frequency domain direct decomposed method (FDDDM), based on time Fourier transform of atomistic heat current, similar to the method by Sääskilahti *et al.*[63] In NEMD, the heat current spectrum $\boldsymbol{Q}(\omega)$ across any virtual or real interface, by which the atoms in the system can be categorized into two parts (named "left" and "right"), can be calculated via

$$\boldsymbol{Q}(\omega) = \sum_{i\in left}\sum_{j\in right} \mathrm{Re}\left[\int_{-\infty}^{+\infty}\left\langle \frac{\partial U_j}{\partial \vec{r}_{ji}}\bigg|_{\tau}\vec{v}_i(0) - \frac{\partial U_i}{\partial \vec{r}_{ij}}\bigg|_{\tau}\vec{v}_j(0)\right\rangle \times e^{i\omega\tau}\left(r_i^0 - r_j^0\right)d\tau\right], \quad (12)$$

where $U$ is the potential, $\vec{r}_i$ and $\vec{v}_i$ are the position and velocity of atom $i$ belong to the left side of the virtual or real interface, and superscript 0 represents the equilibrium position, respectively. The angular brackets represent the time average in NEMD simulations. In this way, the FDDDM can be used to calculate the frequency-dependent thermal boundary conductance, $G(\omega)$, in NEMD simulations by

$$\mathbf{G}(\omega) = -\frac{1}{V_c}\frac{\boldsymbol{Q}(\omega)}{\Delta T}, \quad (13)$$

where $V_c$ is the volume of the control box in a NEMD simulation and $\Delta T$ is the temperature drop at the real or virtual interface. For example, the FDDDM method has been successfully used to study thermal transport across the interface between LJ Ar and heavy Ar crystals with a mass ratio of 10.[64] The $G(\omega)$ between the perfectly abrupt interface, the rough interface (regular Ar and heavy Ar alloyed interface), and the mass graded interface (gradually increase the mass from regular Ar to heavy Ar) is explicitly calculated using Eqs. (12) and (13) and the results are shown in Fig. 8. For low temperature systems, it is widely regarded that the frequency-dependent phonon transmission coefficient, $\alpha(\omega)$, is proportional $G(\omega)$.[63] Therefore, a relatively higher $G(\omega)$ implies a higher $\alpha(\omega)$. Figure 8 indicates that $\alpha(\omega)$ at the

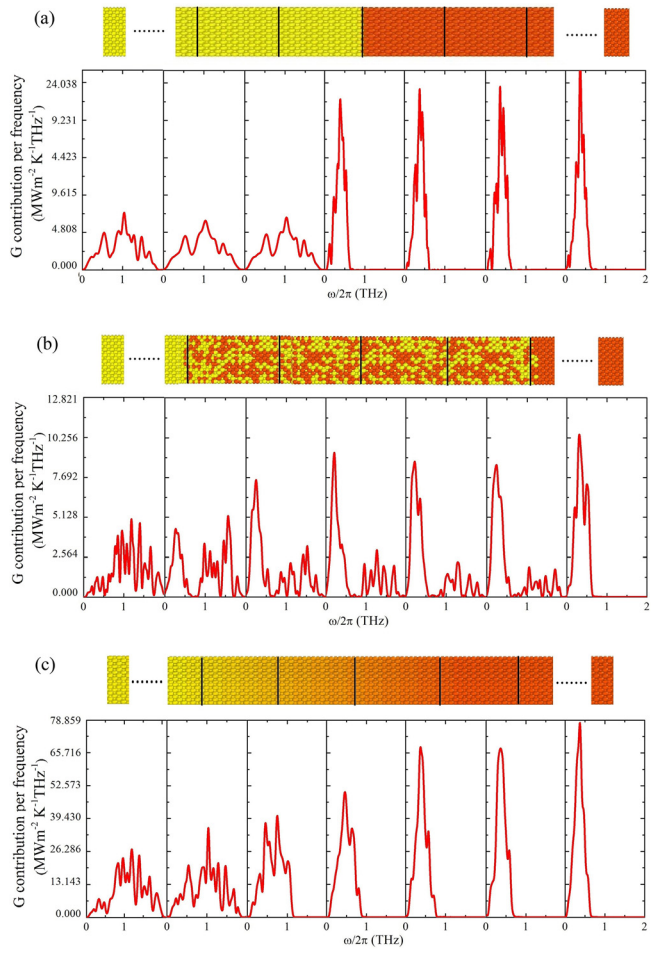


FIG. 8. Comparison of frequency-dependent thermal boundary conductance, $G(\omega)$, between (a) the perfectly abrupt interface, (b) the rough interface, and (c) the mass graded interface. The first and last panels in (a) to (c) represent $G(\omega)$ in the middle of the left and right leads, respectively. The second to fifth panel is $G(\omega)$ at the positions indicated by the black lines in the corresponding structure models. The temperature at the interface is used to obtain $G(\omega)$ (Ref. 64). Reproduced with permission from Y. Zhou, X. Zhang, and M. Hu, Nanoscale **8**, 1994 (2016). Copyright 2016 RSC Publishing.

rough interface is lower than that at the perfectly abrupt interface, while $\alpha(\omega)$ at the mass graded interface is substantially higher than that for the abrupt interface.

Based on the FDDDM, recently Zhou and Hu further developed an explicit theoretical framework by considering the full third-order force constant field to quantify the two- and three-phonon scattering at interfaces.[65] All possible three-phonon scattering processes are taken into consideration by explicitly incorporating the three-body interaction force constants (see schematic Fig. 9). The method is validated by the benchmark bulk Ar, Ar–heavy Ar, and Si-Ge systems. In principle, this method can be further extended to split even higher-order such as fourth-order phonon scattering.

## III. *R* AT DIFFERENT INTERFACES FROM MD SIMULATIONS

### A. *R* at a solid-gas interface

The ability to predict $R$ at a solid-gas interface is of great importance to thermal analysis of a body in a rarefied gas. A gas is regarded as rarefied if the MFP of gas molecules is not negligible compared to the characteristic dimension of the body. A rarefied gas is not necessary to be a gas at very low pressure. For example, the MFP of air molecules at room temperature and 1 atm is only about 100 nm.[66] Though a 100-nm-long MFP seems very short, it is comparable to the dimension of air filled gaps in micro/nanochannels in the cooling element of microelectronics[14,40,67] or MEMS based devices.[68] In this case, the air at 1 atm and near room temperature can be also considered as a rarefied gas and the temperature jump or $R$ at the solid-gas interface must be taken into account in thermal analysis.[68,69]

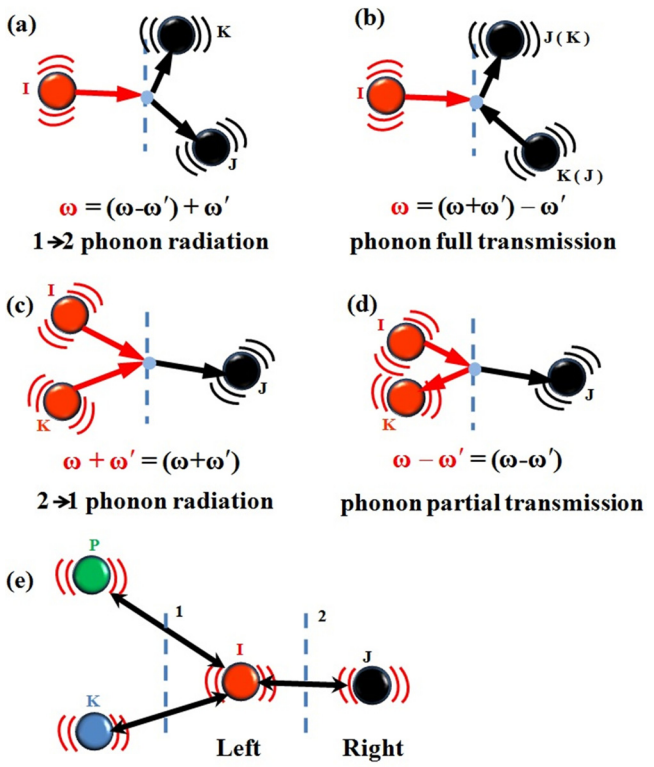


FIG. 9. Schematic of four different types of three-phonon scattering processes at the interface [(a)–(d)]. The situation in bulk materials (e). The blue dashed line represents the interface separating two different materials [(a)–(d)] or an imaginary interface in a bulk material (e) (Ref. 65). Reproduced with permission from Y. Zhou and M. Hu, Phys. Rev. B **95**, 115313 (2017). Copyright 2017 APS Publishing.

Both the EMD and NEMD methods described in Sec. II have been successfully used to determine $R$ at various solid-gas interfaces.[12,14,40,70] The key physical quantity that affects $R$ at the solid-gas interface is the thermal accommodation coefficient (TAC), $\alpha_T$, which quantifies the efficiency of solid-gas heat exchange as

$$\alpha_T = (T_r - T_i)/(T_s - T_i), \tag{14}$$

where $T_i$ and $T_r$ are the temperatures of incident and reflected gas molecules, respectively, and $T_s$ is the solid surface temperature. $\alpha_T = 1$ means that there is a complete thermal equilibration of the incident gas stream with the solid upon reflection. In the temperature jump regime, the kinetic theory of gases relates TAC to the solid-gas thermal boundary conductance, $G$, by[71]

$$G = fk_B N\alpha_T/(2 - \alpha_T), \tag{15}$$

where $f = 4$ for a monoatomic gas such as Ar and Ne, and $f = 6$ for a diatomic gas such as $N_2$ and $O_2$ whose molecules can be approximated as a classical rigid rotor, and $N$ is the collision rate per unit area which is a function of pressure, $P$ and temperature, $T$, and given by[71]

$$N = P/\sqrt{2\pi mk_B T}, \tag{16}$$

where $m$ is the mass of the gas molecule. Based on the relations given in Eqs. (14) through (16), an alternative MD method can be developed to determine $R$ at the solid-gas interface. In this method, one can first calculate the TAC at a given solid-gas interface using MD simulations and then using Eqs. (15) and (16) to predict the $G$ or $R$ at the given solid-gas interface. The simulation results based on the TAC calculations can be used to verify $G$'s found by the EMD and NEMD methods described in Sec. II. Moreover, the MD study of TAC provides more insights into underlying physics in heat transfer at solid-gas interfaces.

For example, Fig. 10 depicts a model system consisting of a solid Au slab in contact with gas Ar at 300 K, 15 bar. The solid-gas interactions are modeled by a LJ potential[12] with a cutoff distance of 11 Å. To determine TAC of gas Ar on an Au surface using Eq. (14), a constant heat flux of 8 MW/m$^2$ is applied across the solid-gas interface via a heat source-sink method described in Sec. II A. After the system reaches a steady state, an imaginary plane is set 11 Å (cutoff distance) away from the solid surface. The incident (or reflected) gas molecules pass through the imaginary plane indicating the start (or finish) of the heat exchange process. The small distance between the plane and surface ensures that the collision between the incident (or reflected) gas molecules and the adjacent gas molecules is rare. The temperature of incident (or reflected) gas Ar molecules is obtained by dividing the average kinetic energy of the incident (or reflected) Ar molecules by $2k_B$.[71] The time-averaged $T_i$, $T_r$ and $T_s$ obtained from the aforementioned NEMD

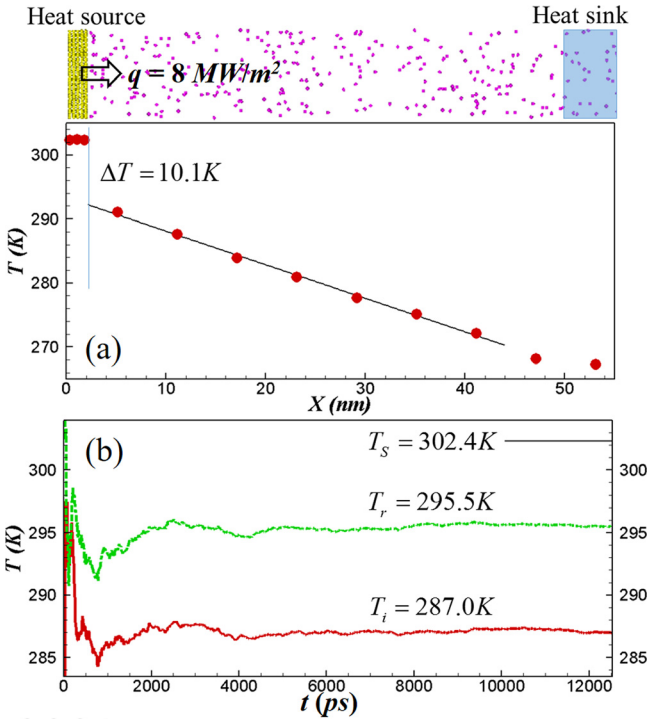


FIG. 10. (a) A snapshot of half of the simulation cell containing solid Au in contact with gas Ar, and the steady-state temperature profile (Ref. 12). Reproduced with permission from Z. Liang and P. Keblinski, Int. J. Heat Mass Transfer **78**, 161 (2014). Copyright 2014 Elsevier. (b) Time-averaged temperature of incident, reflected gas molecules, and solid surface.

simulations are shown in Fig. 10(b). According to the definition of TAC in Eq. (14), $\alpha_T = 0.55 \pm 0.01$ which corresponds to $G = 0.76 \pm 0.02\,\mathrm{MW/m^2\,K}$ according to Eq. (15). The uncertainties are determined from the analysis of eight independent simulation runs. From the same NEMD simulation, one can also find the steady-state temperature profile and the temperature drop the solid-gas interface as shown in Fig. 10(a). Using Eq. (1), one obtains $G = 0.79 \pm 0.04\,\mathrm{MW/m^2\,K}$ which is consistent with the prediction based on TAC calculations. These MD simulation results are obtained at a pressure of 15 bar to get a good statistics and save the computational time. Equations (15) and (16) indicate that $G$ is proportional to the collision rate, which is proportional to pressure. Therefore, the corresponding $G$ at 1 atm and room temperature is about $0.05\,\mathrm{MW/m^2\,K}$, which is 3 to 4 orders of magnitude smaller than the common solid-solid or solid-liquid thermal boundary conductance.

Using the similar MD simulations, one can study effects of various interface parameters such as solid-gas interaction strength, solid-gas atomic mass ratio, solid elastic stiffness,[12] and curvature of the surface[72] on TAC. All these parameters play important roles in solid-gas interfacial heat transfer. The MD simulations offer a fundamental understanding of how these individual parameters affect the nature of gas–solid collisions and thermal conductance at the solid-gas interfaces. The role of individual parameters is often difficult to determine in experiments.[69] The parametric studies can help identify the key interfacial parameters that control the efficiency of solid-gas heat exchange. The MD simulation results are also useful in developing interfaces with enhanced heat transfer under various operation conditions. For example, the recent parametric studies show that a soft surface with a better mass matching between gas molecules and surface atoms will result in more efficient heat exchange at the solid-gas interface.[12] Such a surface can be readily achieved by functionalizing the solid surface with self-assembled monolayers.[12,40]

### B. *R* at a solid-liquid interface

Nanoscale solid-liquid systems, such as nanoparticles or carbon nanotubes (CNT) immersed in a liquid (known as nanofluids), and liquid flows in nanochannels have a variety of applications in hyperthermia-based cancer treatment,[73,74] efficient cooling of microelectronics and engines,[75] and solar thermal heating.[76] The overall thermal behavior in the nanoscale solid-liquid systems is strongly affected by $R$ at the solid-liquid interface, which depends on many parameters such as solid-liquid interaction strength,[77,78] surface structure,[79] and pressure.[80] MD simulation is a very powerful tool to investigate heat transfer across solid-liquid interfaces and has been widely used to calculate $R$ at various solid-liquid interfaces.[15,39,77–83] NEMD determination of $R$ at a planar solid-liquid interface is straightforward. In the most popular scheme, a constant heat flux is applied across the planar interface by a heat source-sink method. After the simulation system reaches a steady state, one extrapolates the linear fit to the temperature profiles in the solid and in the liquid to the interface and finds the temperature drop at the interface. $R$ is then determined by Eq. (1).

Heat transfer in nanoscale solid-liquid systems often involves heat exchange between nanoparticles (or carbon nanotubes) and surrounding liquid. Based on the symmetry of the model system, the way to apply the heat source and heat sink should be modified in MD simulation of heat

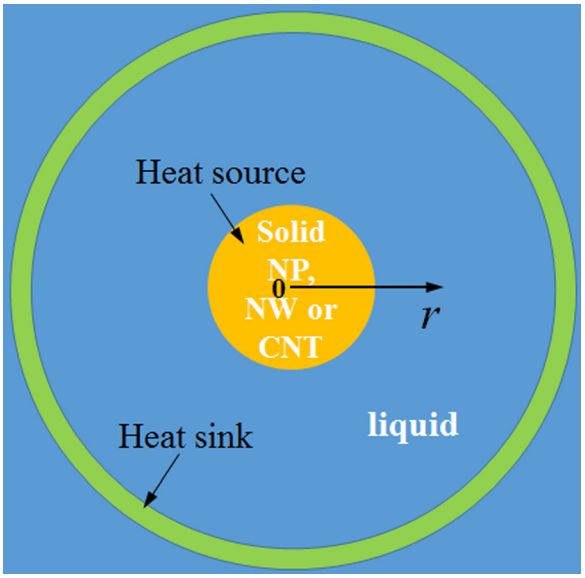


FIG. 11. System schematic depicting the central nanoparticle (nanowire or carbon nanotube) surrounding fluid, and the location of the heat source and sink (Ref. 84). Reproduced with permission from K. Sasikumar, Z. Liang, D. G. Cahill and P. Keblinski, J. Chem. Phys. **140**, 234506 (2014). Copyright 2014 AIP Publishing.

transfer across the curved solid-liquid interface. As shown in Fig. 11, in the study of heat transfer between a nanoparticle (NP) and surrounding liquid, a spherical coordinate system is preferred. After the system reaches the thermal equilibrium, a constant heating power can be added to the NP, and the heat sink can be placed in a spherically symmetric shell centered with the NP to maintain a relatively low temperature in the liquid. Assuming one-dimensional heat transfer and constant thermal conductivity in the liquid, the steady-state temperature profile in the liquid is in the form[2]

$$T(r) = A_1 + B_1/r, \tag{17}$$

where $A_1$ and $B_1$ are constants. Similarly, in the study of heat transfer between a nanowire (NW) or carbon nanotube (CNT) and surrounding liquid, a cylindrical coordinate system is preferred. In this case, the heat source can be applied to the NW or CNT and the heat sink is placed in a cylindrically symmetric shell centered with the NW or CNT. At the steady state, the temperature profile in the liquid is in the form[2]

$$T(r) = A_2 + B_2 \ln r, \tag{18}$$

where $A_2$ and $B_2$ are constants. Since thermal resistance at a solid-liquid interface can be pressure dependent particularly when the solid-liquid interaction strength is small,[80] a barostat should be applied to the system during the NEMD simulation to maintain the system at a desired pressure.

Figure 12 shows an example of NEMD simulation results on heat transfer across an interface between a 10-Å radius NP and surrounding argon-like fluid at a pressure of 20 atm.[84] In the NEMD simulation, the NP is maintained at a high temperature and the liquid in the heat sink is maintained at a temperature lower than the boiling temperature (~243 K) at 20 atm. It is shown in Fig. 12(a) that the steady-state temperature profiles in the surrounding liquid show a good fit to the $T(r) = A_1 + B_1/r$ [i.e., Eq. (17)] form when the nanoparticle temperature ($T_{NP}$) is lower than 1000 K. Extrapolating the fit function to the interface, an evident temperature drop at the interface is found, which manifests a finite $R$ at the solid-liquid interface.

At low nanoparticle temperatures ($T_{NP} < 1000$ K), Fig. 12(b) shows that the $R$ is essentially a constant around 0.014 m$^2$ K/MW ($G \approx 71$ MW/m$^2$ K) which is similar to the typical value of $R$ at a hydrophilic solid-liquid interface found in experiments.[85] At high NP temperatures ($T_{NP} > 1000$ K), a significant departure from the fit ($T(r) = A_1 + B_1/r$) is seen near the solid-liquid interface. The very high temperature gradient near the interface is attributed to the existence of the low-density fluid layer near the NP surface at $T_{NP} > 1000$ K [see Fig. 12(c)]. Such high temperature gradients are not unrealistic. They are achievable in experiments of high-power laser heating of NPs immersed in liquids.[86,87] As fluid density is significantly reduced at high temperatures, the fluid near the NP surface is more gas-like. The $R$ at the solid-gas interface is proportional to the frequency of collision between gas molecules and the solid surface (see Sec. III A). For low-density fluid near the NP surface, the MD simulation results show that the collision rate decreases with the increasing NP temperature. As a result, it is shown in Fig. 12(b) that $R$ at the solid-liquid interface increases with increasing $T_{NP}$ when $T_{NP}$ is higher than 1000 K. It is interesting to see from Fig. 12 that no explosive vaporization occurs even when the temperature of liquid near the hot NP is greater than the spinodal temperature (~310 K) of the model fluid at 20 atm. The stability of such superheated liquid is attributed to the Laplace pressure originating from the density gradient near the NP surface.[84] It is the Laplace pressure that increases the local pressure near the NP and blocks vaporization of superheated liquid around the NP.

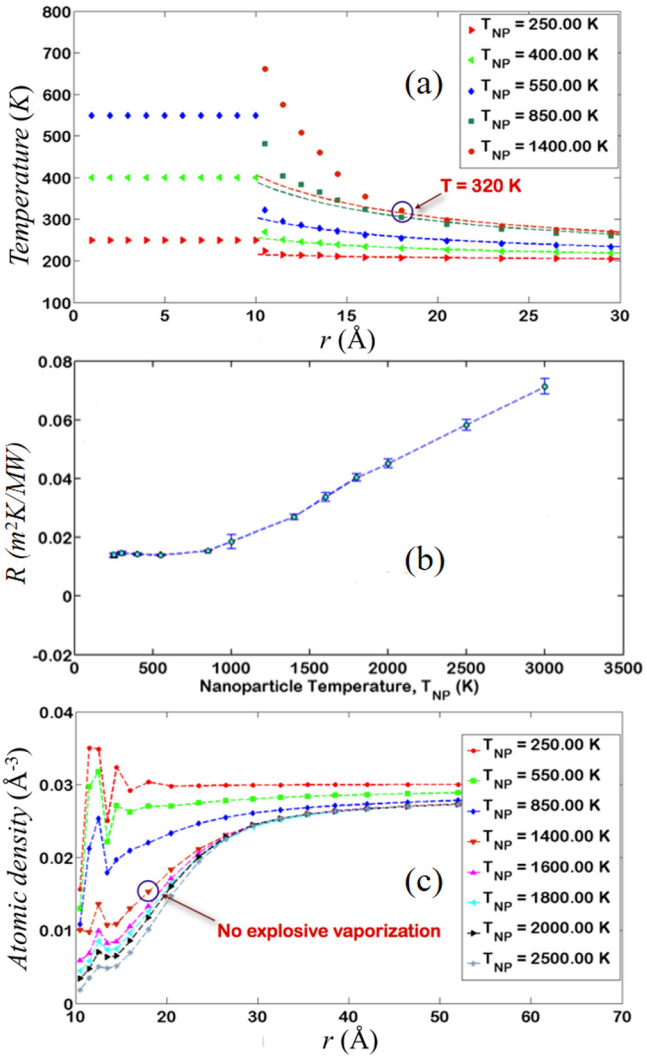


FIG. 12. (a) The steady-state temperature profiles around a 10-Å radius solid particle for different particle temperatures. The dashed lines correspond to a fit based on $T(r) = A_1 + B_1/r$ [i.e., Eq. (17)]. (b) $R$ at the interface between the NP and the surrounding argon-like fluid as a function of NP temperature. The dotted line is used to guide the eye. (c) The steady-state density profiles in the surrounding fluid. The dashed lines are used to guide the eye (Ref. 84). Reproduced with permission from K. Sasikumar, Z. Liang, D. G. Cahill and P. Keblinski, J. Chem. Phys. **140**, 234506 (2014). Copyright 2014 AIP Publishing.

### C. *R* at the solid-solid interface including *R* at interfaces with a nanoscopic confined layer

As power density exponentially goes up, efficient heat dissipation is one of the crucial challenges that limits the development of disruptive microelectronic device

technologies. From a thermal transport point of view, the heat has to go through several technologically necessary layers at the transistor level and then go through several layers in external packaging. This motivated us to manage the heat transfer across solid-solid interfaces. Detailed analysis shows that 50% of total thermal resistance comes from interfaces, making interfacial thermal transport the dominant factor in the performance of electronic cooling.

In the initial studies of interfacial thermal transport, only two materials in contact were considered, and the heat travels from one material to the other [see the schematic in Fig. 13(a)]. In this case, the overall thermal boundary resistance is simply the resistance at the interface between two materials. In this line, people have developed tremendous methods to enhance the heat conduction across single interfaces. The major efforts were dedicated to tailoring the surface/interface conditions, such as chemical functionalization using small molecules (e.g., self-assembled monolayer interfaces),[88] introducing strong chemical covalent bonding at interfaces,[50] nanostructuring the surfaces,[89] and by pressure.[19]

Now let us incorporate a third material between two slabs of materials. We call it the thermal interface material (TIM) [see schematic Fig. 13(b)]. In this case, the overall thermal boundary resistance is the sum of two interfacial resistances plus the resistance of the TIM. Usually in this case, the overall thermal resistance will increase, due to the finite thermal conductivity of the TIM and the additional interfacial resistance. This is especially true at the continuum scale. However, at the nanoscale, as the thickness of the confined TIM becomes smaller and smaller, nanoconfinement can strongly affect the thermal conductivity of the TIM and also strongly affect the nearby interfacial resistance. Therefore, it is possible to reduce the overall thermal boundary resistance as compared with the two material cases.

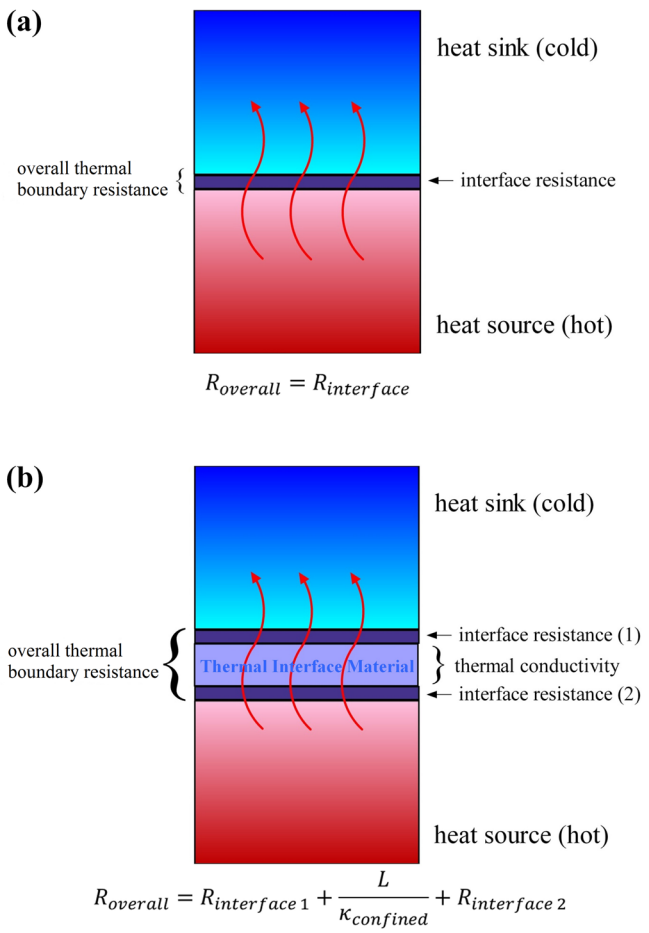


FIG. 13. Schematic of interfacial thermal transport across (a) a single interface and (b) confined interfaces (the material confined between two bulk slabs is called thermal interface material).

Here, the idea of nanoconfinement is first applied to heat transfer across the solid-solid interface by confining a thin liquid layer.[90] The MD model system consists of two neighboring hydrophilic quartz slabs confining a water layer. Surprisingly, a significant increase and a non-intuitive, non-monotonic dependence of the overall thermal boundary conductance between the quartz surfaces on the water layer thickness were observed. The mechanism of the thermal conductance peak occurring at the sub-monolayer water stems from the freezing of water molecules at extremely confined conditions and the excellent match of vibrational states between trapped water and hydrophilic headgroups on the two contact surfaces. These results pave the way for incorporating polar molecules into hydrophilic interfaces as a very promising route to enhance the thermal transport through thermally smooth connection of neighboring interfaces.

The second example we take is the SiC|GaN interface.[57,91] As we all know, the GaN high electron mobility transistor is very attractive for high power amplifiers. The near-junction heat flux involved could be as large as several kW/mm$^2$, which is at least three orders of magnitude higher than that in typical supercomputers. Thus, efficient near-junction heat dissipation is crucial to the reliability of GaN devices. By incorporating a nanoscopic AlN layer between SiC and GaN, the MD simulation[57] demonstrated that the overall thermal conductance is generally 45%–55% higher than that for the bare interface, especially for a subnanometer AlN layer. There are two mechanisms responsible for this. First, the strong nanoconfinement effect results in very high thermal conductivity of the AlN layer with the decrease of thickness. Second, as we discussed in Sec. II D 2 the confined AlN serves as a phonon bridge to connect GaN and SiC surfaces. Putting the two mechanisms together, we can understand why the overall thermal conductance increases with the thickness of the AlN layer decreasing.

Another example of the interfacial nanoconfinement effect is the mass graded interface (see Fig. 8). It was found from MD simulations[64] that by using the mass graded interface to connect two materials, the overall thermal boundary resistance is reduced by 6 folders, as compared with the perfectly abrupt interface. The mass graded interface is also much better than the alloyed interface in terms of improving interfacial thermal transport. The mechanism mainly comes from the two different regimes of interfacial heat transfer across the rough interface, which originates from the competition between phonon scattering and the interface thickness. When the thickness is large enough, there is enough space for high-frequency phonons to scatter, which results in a greater thermal boundary resistance. When the thickness is reduced to the nanoscale, there is not enough space for phonon scattering and thus, the thermal boundary resistance

decreases. In addition, the mass graded interface can achieve a high transmission coefficient of both LA and TA phonon modes over a large frequency range. A similar phenomenon was also reported in a single solid layer confined between two solid slabs.[28] The MD simulation of a more realistic $Ge^{70}$-$Ge^{76}$ interface shows that the overall thermal boundary conductance for the mass graded interface is about two times of that for the abrupt interface.[64] The mass or composition graded interface in semiconductor components can be fabricated in experiment by chemical vapor deposition (CVD).[92,93]

## IV. OTHER MD METHODS

Before closing, we would also like to discuss some other MD methods that emerge in recent years. First, recently the approach-to-equilibrium molecular dynamics (AEMD)[94–97] was proposed to calculate the lattice thermal conductivity and thermal boundary resistance during the transient regime of approach to equilibrium from an initial condition of the non-uniform temperature profile. In the AEMD determination of thermal boundary resistance, $R$, the two materials in contact are first equilibrated at two different temperatures with a temperature difference of $\Delta T$. Then, an NVE (the number of particles, volume and total energy of the system are conserved) simulation is carried out to let the bi-material system attain the thermal equilibrium. During the AEMD simulation, one can record the instantaneous average temperature in each of the materials, and the decay of the temperature difference, $\Delta T$, as a function of time, $t$. Such a procedure is analogous to the experimental laser-flash method[98] in which a highly localized temperature transient is created by short-pulsed laser irradiation.

In the single-exponential limit,[95,97] $\Delta T \propto \exp(-t/\tau)$, the total thermal resistance, $R_{\text{tot}}$, of the bi-material system is obtained as[95]

$$R_{tot} = \frac{A}{C_V}\int_0^{\infty}\frac{\Delta T(t)}{\Delta T(0)}dt = \frac{A\tau}{C_V}, \tag{19}$$

where $A$ is the cross section area, and $C_V$ is the heat capacity of the model system. If a model structure contains material 1 with the length of $L_1$ in contact with material 2 with the length of $L_2$, and the PBCs are applied in the heat flow direction, $R_{\text{tot}}$ is the sum of thermal resistances in the two materials and that at the interface

$$R_{tot} = \frac{L_1}{k_1} + 2R + \frac{L_2}{k_2}, \tag{20}$$

where $k_1$ and $k_2$ are the thermal conductivity of material 1 and material 2, respectively. In Eq. (20), the thermal boundary resistance, $R$, doubled because of the PBCs. $k_1$ and $k_2$ in Eq. (20) can be found by separate AEMD simulations in a pure system containing only material 1 or material 2.[97] Using the aforementioned AEMD method, Lampin *et al.*[95] studied the $R$ at $c$-Si|$a$-$SiO_2$ interfaces. Figure 14 shows that the time-decay of the $\Delta T$ for the $c$-Si|$a$-$SiO_2$ interfaces follows a single decaying exponential when the system approaches thermal equilibrium. With the exponential decay

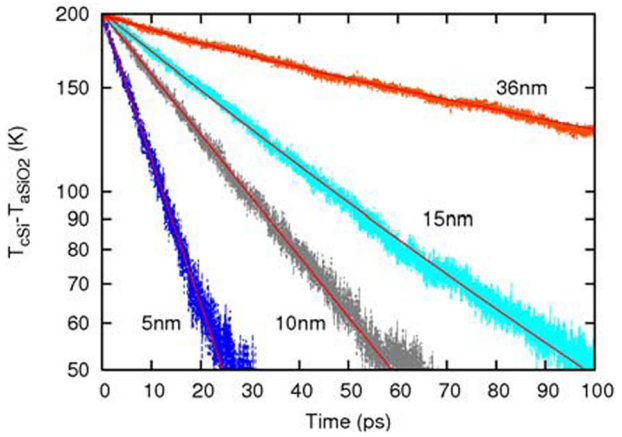


FIG. 14. Semi-log plot of the temperature difference ΔT vs. time, from NVE MD with the AEMD method, after initial equilibration at 600 K ($c$Si) and 400 K ($a$$SiO_2$). Cross section 19.4 $nm^2$; constant crystal block length, $L_C = 150$ nm; variable $a$$SiO_2$ block length, $L_a = 5$, 10, 15, and 36 nm. The single-exponential decay times extracted by linear fit (red lines) are: $\tau = 18$ ps for $L_a = 5$ nm; 42 ps for 10 nm; 71 ps for 15 nm; and 245 ps for 36 nm (Ref. 95). Reproduced with permission from E. Lampin, Q.-H. Nguyen, P. A. Francioso, and F. Cleri, Appl. Phys. Lett. **100**, 131906 (2012). Copyright 2012 AIP Publishing.

time, $\tau$, extracted from $\Delta T$ *vs.* $t$, one can determine $R_{\text{tot}}$ using Eq. (19), and eventually find the value of $R$ using Eq. (20). Using the AEMD method, Lampin *et al.* obtained $R = 0.4$ $m^2$ K/GW, which is comparable to the value found in experiment.[99] A similar AEMD method is also applied to study $R$ at other interfaces such as Si/Ge interfaces.[94]

The physical basics, the robustness, and the accuracy of the AEMD method have been demonstrated to be independent of the arbitrary simulation parameters. The most significant feature of this method is that it is computationally economic, making investigation of large systems or long time scales (that is well beyond the classical MD) possible. However, since AEMD is based on the transient process which is different from steady state NEMD and pure EMD, how to extract phonon mode information from AEMD such as relaxation time, phonon mode contribution is still unavailable. This needs further development in the near future.

Second, first-principles MD (FPMD) would play a more important role than ever before, as computing capacity is boosted. In FPMD, the interatomic potential is obtained from first principles by using a quantum mechanics method, such as density functional theory.[100] The significant advantage of FPMD is that it does not rely on the explicit interatomic potential, which is not available for many complex systems. Currently, both first-principles equilibrium molecular dynamics (FPEMD) and first-principles nonequilibrium molecular dynamics (FPNEMD) have been used to calculate the lattice thermal conductivity of complex systems such as perovskite solar cells,[101,102] where empirical interatomic potential is not easy to figure out. Since FPMD is in principle the same as classical MD, almost all the aforementioned postprocessing approaches such as SED, TDNMA, and FDDDM can be straightforwardly translated to FPMD. FPMD can be also coupled with the aforementioned AEMD to study thermal transport in nanomaterials.[103] While FPMD has no limitation in choosing the systems, i.e., no matter

what elements and structures are involved, the biggest drawback of FPMD is its prohibitive computational cost. This implies that FPMD is limited to small systems (up to ~1000 atoms) and short times (up to several hundreds of ps). Due to this limit, FPMD was only applied to a system containing a few hundred atoms to calculate the thermal conductivity of materials.[101–104] The determination of $R$ at material interfaces usually requires a simulation cell containing $10^4$–$10^5$ atoms. As a result of the high computational cost, FPMD has not been applied to determine $R$ at material interfaces so far. With the fast growth in computing power, we expect that FPMD will be used to study thermal transport across material interfaces in the future.

## V. SUMMARY

The MD simulation is a very powerful tool for studying heat transfer across material interfaces. Both EMD and NEMD methods can be used to determine the magnitude of thermal resistance at various material interfaces. If the finite size effects are treated properly, the thermal boundary resistance, $R$, predicted from the EMD method should be consistent with that from the NEMD method. Nevertheless, the correct determination of $R$ from the EMD method is generally more challenging than that from the NEMD method as extra caution must be exercised on effects associated with finite heat capacity of the simulation domain and the definition of the location of the interface in the EMD determination of $R$ at a rough interface or an interface with an adsorbed layer. At solid-gas interfaces, the kinetic theory of gases relates $R$ to the TAC of gas molecules on a solid surface. The TAC quantifies the solid-gas heat exchange efficiency and can be readily obtained from MD simulations. The simulation results showed that the thermal resistances at solid-gas interfaces predicted from EMD and NEMD simulations are consistent with that from the kinetic gas theory. At solid-liquid interfaces, the MD simulation can be used to study effects of a variety of interfacial parameters such as solid-liquid interaction strength, pressure, and surface structure on $R$. The MD study of high heat flux across a curved solid-liquid interface is related to the experiment of high-power laser heating of NPs immersed in liquids. The thermal resistance at a solid-liquid interface is also strongly affected by the curvature of the interface and temperature of the solid as vaporization could occur in liquid near a very hot surface. An important issue in MD determination of thermal resistance at solid-solid interfaces is that the finite size effects must be treated properly. To determine thermal resistance at an isolated solid-solid interface, the simulation cell size must be large enough to remove the artificial size effect in the MD model. MD simulation results showed that introduction of very rough external boundaries to the model structure can significantly suppress the size effects and reduce the computational cost for obtaining a size-converged $R$. Lack of proper account for the size effects could lead to incorrect predictions about the role of different interface parameters in $R$.

The MD simulation is also very useful in analyzing and understanding interfacial phonon transport phenomena. The detailed information on how individual phonons interact with the interface such as the frequency-dependent phonon transmission coefficient can be obtained from the WPD simulation. One drawback of the WPD simulation is that the simulation was all conducted at a temperature of 0 K so far. More effort can be put into extending the current WPD model to study phonon-interface interactions at finite temperatures in the future. If the interfacial phonon scattering is mainly diffuse, the phonon transmission coefficient can be qualitatively determined by comparing the VDOSs in materials on two sides of the interface. A large overlap between the two VDOSs indicates a higher transmission coefficient and a lower thermal resistance at the interface. Hence, the VDOS, which is usually obtained from EMD simulations, can be used to understand the enhanced or reduced interfacial thermal transport under different interface conditions. While the thermal boundary conductance determined from the conventional EMD and NEMD methods includes contributions from all phonon frequencies and modes, the frequency-dependent thermal boundary conductance, $G(\omega)$, can be obtained from the FDDDM. $G(\omega)$ can help identify the mode and frequency of phonons that make main contribution to the interfacial thermal transport.

The MD simulation only accounts for interfacial thermal transport by phonons. At metal/nonmetal interfaces, however, electron-phonon coupling at the interface could also affect the thermal boundary resistance.[105,106] The MD model alone cannot handle the electronic contribution to the interfacial thermal transport. In this case, one needs to combine the MD model with other approaches such as the two-temperature model[105–107] to include the electron-phonon coupling effect in interfacial thermal transport.

## ACKNOWLEDGMENTS

Z.L. acknowledges the eXtreme Science and Engineering Discovery Environment (XSEDE) for providing supercomputer resources for MD simulations. M.H. acknowledges the Start-Up Funding provided by the University of South Carolina.

[1]D. G. Cahill, W. K. Ford, K. E. Goodson, G. D. Mahan, A. Majumda, H. J. Maris, R. Merlin, and S. R. Phillpot, J. Appl. Phys. **93**, 793 (2003).
[2]Y. A. Cengel and A. J. Ghajar, *Heat and Mass Transfer, Fundamentals & Applications*, 5th ed. (McGraw Hill Education, 2014).
[3]A. M. Marconnet, M. Asheghi, and K. E. Goodson, J. Heat Transfer **135**, 061601 (2013).
[4]B.-Y. Nguyen, G. Celler, and C. Mazure, J. Integr. Circuit Syst. **4**, 51 (2009); available at http://www.sbmicro.org.br/jics/html/artigos/vol4no2/01.pdf.
[5]M. Lutz, A. Partridge, P. Gupta, N. Buchan, E. Klaassen, J. McDonald, and K. Petersen, in *14th International Conference on Solid-State Sensors, Actuators and Microsystems Conference* (IEEE, Lyon, France, 2007), p. 49.
[6]E. T. Swartz and R. O. Pohl, Rev. Mod. Phys. **61**, 605 (1989).
[7]W. Eisenmenger, "Phonon scattering at surfaces and interfaces," in *Phonon Scattering in Condensed Matter V*, edited by A. C. Anderson and J. P. Wolfe (Springer, Berlin/Heidelberg/New York, 1986), p. 204.
[8]E. T. Swartz, "Solid-solid thermal boundary resistance," Ph.D. thesis (Cornell University, 1987).
[9]X. W. Zhou, R. E. Jones, C. J. Kimmer, J. C. Duda, and P. E. Hopkins, Phys. Rev. B **87**, 094303 (2013).
[10]Z. Liang and P. Keblinski, Phys. Rev. B **90**, 075411 (2014).

[11]T. S. English, J. C. Duda, J. L. Smoyer, D. A. Jordan, P. M. Norris, and L. V. Zhigilei, Phys. Rev. B **85**, 035438 (2012).
[12]Z. Liang and P. Keblinski, Int. J. Heat Mass Transfer **78**, 161 (2014).
[13]R. Prasher, Appl. Phys. Lett. **94**, 041905 (2009).
[14]Z. Liang, W. Evans, and P. Keblinski, Phys. Rev. E **87**, 022119 (2013).
[15]N. Shenogina, R. Godawat, P. Keblinski, and G. Garde, Phys. Rev. Lett. **102**, 156101 (2009).
[16]H. K. Lyeo and D. G. Cahill, Phys. Rev. B **73**, 144301 (2006).
[17]P. E. Hopkins, P. M. Norris, and R. J. Stevens, J. Heat Transfer **130**, 022401 (2008).
[18]E. S. Landry and A. J. H. McGaughey, Phys. Rev. B **80**, 165304 (2009).
[19]M. Shen, W. Evans, D. Cahill, and P. Keblinski, Phys. Rev. B **84**, 195432 (2011).
[20]W.-P. Hsieh, A. S. Lyons, E. Pop, P. Keblinski, and D. G. Cahill, Phys. Rev. B **84**, 184107 (2011).
[21]A. Pham, M. Barisik, and B. Kim, J. Chem. Phys. **139**, 244702 (2013).
[22]R. J. Stevens, L. V. Zhigilei, and P. M. Norris, Int. J. Heat Mass Transfer **50**, 3977 (2007).
[23]B. Ni, T. Watanabe, and S. R. Phillpot, J. Phys.: Condens. Matter **21**, 084219 (2009).
[24]S. Ju, X. Liang, and S. Wang, J. Phys. D: Appl. Phys. **43**, 085407 (2010).
[25]L. Sun and J. Y. Murthy, J. Heat Transfer **132**, 102403 (2010).
[26]E. S. Landry and A. J. H. McGaughey, J. Appl. Phys. **107**, 013521 (2010).
[27]X.-W. Zhou, R. E. Jones, P. E. Hopkins, and T. E. Beechem, Phys. Chem. Chem. Phys. **16**, 9403 (2014).
[28]Z. Liang and H.-L. Tsai, J. Phys.: Condens. Matter **23**, 495303 (2011).
[29]P. Jund and R. Jullien, Phys. Rev. B **59**, 13707 (1999).
[30]H. J. C. Berendsen, J. P. M. Postma, W. F. Van Gunsteren, A. Di Nola, and J. R. Haak, J. Chem. Phys. **81**, 3684 (1984).
[31]S. A. Adelman and J. D. Doll, J. Chem. Phys. **64**, 2375 (1976).
[32]D. Frenkel and B. Smit, *Understanding Molecular Simulation* (Academic Press, San Diego, 2002).
[33]Z. Liang, K. Sasikumar, and P. Keblinski, Phys. Rev. Lett. **113**, 065901 (2014).
[34]R. E. Jones, J. C. Duda, X. W. Zhou, C. J. Kimmer, and P. E. Hopkins, Appl. Phys. Lett. **102**, 183119 (2013).
[35]T. Watanabe, B. Ni, S. R. Phillpot, P. K. Schelling, and P. Keblinski, J. Appl. Phys. **102**, 063503 (2007).
[36]D. G. Cahill, P. V. Braun, G. Chen, D. R. Clarke, S. Fan, K. E. Goodson, P. Keblinski, W. P. King, G. D. Mahan, A. Majumdar, H. J. Maris, S. R. Phillpot, E. Pop, and L. Shi, Appl. Phys. Rev. **1**, 011305 (2014).
[37]L. Puech, G. Bonfait, and B. Castaing, J. Low Temp. Phys. **62**, 315 (1986).
[38]Y. Chalopin, K. Esfarjani, A. Henry, S. Volz, and G. Chen, Phys. Rev. B **85**, 195302 (2012).
[39]J.-L. Barrat and F. Chiaruttini, Mol. Phys. **101**, 1605 (2003).
[40]Z. Liang, W. Evans, T. Desai, and P. Keblinski, Appl. Phys. Lett. **102**, 061907 (2013).
[41]S. Merabia and K. Termentzidis, Phys. Rev. B **86**, 094303 (2012).
[42]Y. K. Koh, Y. Cao, D. G. Cahill, and D. Jena, Adv. Funct. Mater. **19**, 610 (2009).
[43]P. K. Schelling, S. R. Phillpot, and P. Keblinski, Appl. Phys. Lett. **80**, 2484 (2002).
[44]P. K. Schelling, S. R. Phillpot, and P. Keblinski, J. Appl. Phys. **95**, 6082 (2004).
[45]Z. Liang and P. Keblinski, Phys. Rev. B **93**, 054205 (2016).
[46]B. Deng, A. Chernatynskiy, M. Khafizov, D. H. Hurley, and S. R. Phillpot, J. Appl. Phys. **115**, 084910 (2014).
[47]M. Hu, P. Keblinski, J.-S. Wang, and N. Raravikar, J. Appl. Phys. **104**, 083503 (2008).
[48]H. Bao, C. Shao, S. Luo, and M. Hu, J. Appl. Phys. **115**, 053524 (2014).
[49]C. Shao, Q. Rong, M. Hu, and H. Bao, J. Appl. Phys. **122**, 155104 (2017).
[50]M. Hu, P. Keblinski, and P. K. Schelling, Phys. Rev. B **79**, 104305 (2009).
[51]J. A. Thomas, J. E. Turney, R. M. Iutzi, C. H. Amon, and A. J. H. McGaughey, Phys. Rev. B **81**, 081411(R) (2010).
[52]A. S. Henry and G. Chen, J. Comput. Theor. Nanosci. **5**, 141 (2008).
[53]S. C. Huberman, J. M. Larkin, A. J. H. McGaughey, and C. H. Amon, Phys. Rev. B **88**, 155311 (2013).
[54]J. M. Larkin and A. J. H. McGaughey, J. Appl. Phys. **114**, 023507 (2013).
[55]Y. Chalopin and S. Volz, Appl. Phys. Lett. **103**, 051602 (2013).
[56]M. P. Allen and D. J. Tildesley, *Computer Simulation of Liquid* (Oxford University Press, Oxford, 2000).
[57]M. Hu, X. Zhang, D. Poulikakos, and C. P. Grigoropoulos, Int. J. Heat Mass Transfer **54**, 5183 (2011).
[58]Y. Zhou, X. Zhang, and M. Hu, Phys. Rev. B **92**, 195204 (2015).
[59]J. H. Irving and J. G. Kirkwood, J. Chem. Phys. **18**, 817 (1950).
[60]D. Torii, T. Nakano, and T. Ohara, J. Chem. Phys. **128**, 044504 (2008).
[61]T. Ohara, J. Chem. Phys. **111**, 9667 (1999).
[62]Y. Zhou and M. Hu, Phys. Rev. B **92**, 195205 (2015).
[63]K. Sääskilahti, J. Oksanen, S. Volz, and J. Tulkki, Phys. Rev. B **91**, 115426 (2015).
[64]Y. Zhou, X. Zhang, and M. Hu, Nanoscale **8**, 1994 (2016).
[65]Y. Zhou and M. Hu, Phys. Rev. B **95**, 115313 (2017).
[66]S. Jennings, J. Aerosol. Sci. **19**, 159 (1988).
[67]S. Song, M. M. Yovanovich, and F. O. Goodman, J. Heat Transfer **115**, 533 (1993).
[68]L. Biswal, S. K. Som, and S. Chakraborty, Int. J. Heat Mass Transfer **50**, 1248 (2007).
[69]G. S. Springer, *Heat Transfer in Rarefied Gases* (Academic Press, New York, 1971), p. 164.
[70]M. Hu, S. Shenogin, P. Keblinski, and N. Raravikar, Appl. Phys. Lett. **90**, 231905 (2007).
[71]F. O. Goodman and H. Y. Wachman, *Dynamics of Gas-Surface Scattering* (Academic Press, New York, 1976), pp. 23–31.
[72]L. Hu and A. J. H. McGaughey, J. Phys. Chem. C **117**, 11804 (2013).
[73]D. P. O'Neal, L. R. Hirsch, N. J. Halas, J. D. Payne, and J. L. West, Cancer Lett. **209**, 171 (2004).
[74]L. R. Hirsch, R. J. Stafford, J. A. Bankson, S. R. Sershen, B. Rivera, R. E. Price, J. D. Hazle, N. J. Halas, and J. L. West, Proc. Natl. Acad. Sci. U.S.A. **100**, 13549 (2003).
[75]P. Keblinski, J. A. Eastman, and D. G. Cahill, Mater. Today **8**, 36 (2005).
[76]O. Neumann, A. S. Urban, J. Day, S. Lal, P. Nordlander, and N. J. Halas, ACS Nano **7**, 42 (2013).
[77]L. Xue, P. Keblinski, S. R. Phillpot, S. U. S. Choi, and J. A. Eastman, J. Chem. Phys. **118**, 337 (2003).
[78]M. Barisik and A. Beskok, Int. J. Therm. Sci. **77**, 47 (2014).
[79]M. Shibahara, T. Kunugi, K. Muko, and M. Katsuki, Nanoscale Microscale Thermophys. Eng. **10**, 197 (2006).
[80]K. Issa and A. Mohamad, in Proceedings of the 3rd International Conference on Nanotechnology: Fundamentals and Applications, Paper No. 332 (2012).
[81]D. Torii, T. Ohara, and K. Ishida, J. Heat Transfer **132**, 012402 (2010).
[82]L. Xue, P. Keblinski, S. R. Phillpot, S. U. S. Choi, and J. A. Eastman, Int. J. Heat Mass Transfer **47**, 4277 (2004).
[83]Z. Liang, W. Evans, and P. Keblinski, J. Chem. Phys. **141**, 014706 (2014).
[84]K. Sasikumar, Z. Liang, D. G. Cahill, and P. Keblinski, J. Chem. Phys. **140**, 234506 (2014).
[85]Z. B. Ge, D. G. Cahill, and P. V. Baun, Phys. Rev. Lett. **96**, 186101 (2006).
[86]M. Hu, P. Hristina, and G. V. Hartland, Chem. Phys. Lett. **391**, 220 (2004).
[87]A. Plech, V. Kotaidis, S. Grésillon, C. Dahmen, and G. von Plessen, Phys. Rev. B **70**, 195423 (2004).
[88]L. Hu, L. Zhang, M. Hu, J.-S. Wang, B. Li, and P. Keblinski, Phys. Rev. B **81**, 235427 (2010).
[89]J. V. Goicochea, M. Hu, B. Michel, and D. Poulikakos, J. Heat Transfer **133**, 082401 (2011).
[90]M. Hu, J. V. Goicochea, B. Michel, and D. Poulikakos, Nano Lett. **10**, 279 (2010).
[91]M. Hu and D. Poulikakos, Int. J. Heat Mass Transfer **62**, 205 (2013).
[92]C. L. Wu, W. C. Hsu, H. M. Shieh, and W. C. Liu, Appl. Phys. Lett. **64**, 3207 (1994).
[93]P. Ferrando-Villalba, A. F. Lopeandía, F. X. Alvarez, B. Paul, C. de Tomás, M. I. Alonso, M. Garriga, A. R. Goñi, J. Santiso, and G. Garcia, Nano Res. **8**, 2833 (2015).
[94]K. R. Hahn, M. Puligheddu, and L. Colombo, Phys. Rev. B **91**, 195313 (2015).
[95]E. Lampin, Q.-H. Nguyen, P. A. Francioso, and F. Cleri, Appl. Phys. Lett. **100**, 131906 (2012).
[96]C. Melis and L. Colombo, Phys. Rev. Lett. **112**, 065901 (2014).
[97]E. Lampin, P. L. Palla, P.-A. Francioso, and F. Cleri, J. Appl. Phys. **114**, 033525 (2013).
[98]W. J. Parker, R. J. Jenkins, C. P. Butler, and G. L. Abbott, J. Appl. Phys. **32**, 1679 (1961).

[99]D. H. Hurley, M. Khafizov, and S. L. Shinde, J. Appl. Phys. **109**, 083504 (2011).
[100]W. Kohn and L. J. Sham, Phys. Rev. **140**, A1133 (1965).
[101]S.-Y. Yue, X. Zhang, G. Qin, J. Yang, and M. Hu, Phys. Rev. B **94**, 115427 (2016).
[102]G. Qin, X. Zhang, S.-Y. Yue, Z. Qin, H. Wang, Y. Han, and M. Hu, Phys. Rev. B **94**, 165445 (2016).
[103]S. Illera, M. Pruneda, L. Colombo, and P. Ordejón, Phys. Rev. Mater. **1**, 044006 (2017).
[104]J. Kang and L.-W. Wang, Phys. Rev. B **96**, 020302(R) (2017).
[105]A. Majumdar and P. Reddy, Appl. Phys. Lett. **84**, 4768 (2004).
[106]Y. Wang, X. L. Ruan, and A. K. Roy, Phys. Rev. B **85**, 205311 (2012).
[107]Z. Lin, R. A. Johnson, and L. V. Zhigilei, Phys. Rev. B **77**, 214108 (2008).